

## Supporting Information

### **A Nanoscopic View of Photoinduced Charge Transfer in Organic Nanocrystalline Heterojunctions**

Qian Zhang<sup>±</sup>, Sidney R. Cohen<sup>†</sup>, Irit Rosenhek-Goldian<sup>†</sup>, Daniel Amgar<sup>‡</sup>, Omri Bar-Elli<sup>‡</sup>, Yael Tsarfati<sup>±</sup>, Tatyana Bendikov<sup>†</sup>, Linda J W Shimon<sup>†</sup>, Yishay Feldman<sup>†</sup>, Mark Iron<sup>†</sup>, Haim Weissman<sup>±</sup>, Igal Levine<sup>§</sup>, Dan Oron<sup>‡</sup>, and Boris Rybtchinski<sup>±\*</sup>

Department of <sup>±</sup>Organic Chemistry, <sup>†</sup>Chemical Research Support, <sup>‡</sup>Physics of Complex Systems, and <sup>§</sup>Materials and Interfaces, Weizmann Institute of Science, Rehovot 7610001, Israel.

E-mail: [boris.rybtchinski@weizmann.ac.il](mailto:boris.rybtchinski@weizmann.ac.il)

## **General Information**

**Electrochemical** experiments were carried out using a CHI660A electrochemical workstation inside a faraday cage. A Pt electrode with a diameter of 5 mm was used as the working electrode, Ag/AgCl as the reference electrode, and a Pt wire as the counter electrode. 0.1 M tetrabutylammonium hexafluorophosphate (TBAFP) in dry dichloromethane (DCM) was used as the supporting electrolyte. All electrochemical measurements were performed under a nitrogen atmosphere. The investigated materials were dissolved in DCM to a concentration of  $10^{-5}$  M, CV was measured in the range of 0.8 to  $-0.9$  V. Ferrocene was added as an internal reference. Energy levels of the PDI molecular frontier orbitals were calculated from electrochemical measurements according to  $E_{\text{LUMO}}$  (vs. vacuum, eV) =  $-(E_{\text{CV}} - E_{\text{Fc/Fc}^+}) - 4.8$  eV and  $E_{\text{HOMO}}$  (vs. vacuum, eV) =  $E_{\text{LUMO}} - E_{\text{g}}^{\text{solution}}$ .  $E_{\text{CV}}$  and  $E_{\text{Fc/Fc}^+}$  are the onset of the first reducing peak of PDIs and the onset of the oxidizing peak of ferrocene.  $E_{\text{HOMO}}$ ,  $E_{\text{LUMO}}$ , and  $E_{\text{g}}^{\text{solution}}$  are the energy of the highest occupied molecular orbital (HOMO), the energy of the lowest unoccupied molecular orbital (LUMO) and the optical band-gap (determined from the crossing point of normalized absorption and fluorescence spectra) of the molecules in chloroform.

**X-Ray Diffraction (XRD)** measurements were carried out in reflection mode using an Ultima III (Rigaku) diffractometer equipped with a sealed Cu anode operating at 40 kV and 40 mA. A flat graphite monochromator and a scintillation detector were aligned in the diffracted beam. Asymmetric  $2\theta$  scans with a fixed incident angle at  $1.8^\circ$  were performed using parallel-beam optics in the range  $2^\circ$ - $30^\circ$  of  $2\theta$  angles.

**Transmission Electron Microscopy (TEM)** samples were prepared on 200-mesh gold grid (bare or Quantifoil 2/2). Configuration-I sample was prepared by first depositing 70-nm thick CuPc film, then DMP-PDI ONCs were overlaid onto the CuPc film by Langmuir-Schaeffer method. Configuration-II sample was prepared by collecting the CuPc-decorated PDI ONCs directly onto a gold TEM grid or onto the carbon film of the Quantifoil grid through Langmuir-Schaeffer method. Imaging was performed using Tecnai T12 transmission electron microscope operated at 120 kV, equipped with a TVIPS TemCam-XF416 CMOS digital camera. Low dose mode was used in order to minimize damage to the organic materials. The bare gold grid meshes were aligned to the tilt axis of the stage to enable optimal viewing angles of the deposited materials on the walls of the gold mesh.

**Macroscopic CPD and surface photovoltage (SPV)** measurements were performed with a custom-built Kelvin probe system with a Besocke Delta-Phi controller and a gold mesh probe. Sample illumination was performed using a controllable intensity 360 W halogen lamp. All measurements were performed in a nitrogen-filled glovebox with nominal O<sub>2</sub> and H<sub>2</sub>O levels below 5 ppm at a pressure of 1.0035 bar.

**Time-resolved fluorescence lifetimes** were determined using a biexponential fit of the decay curve

$$f(t) = A_1 \cdot \exp(\Gamma_1 \cdot t) + A_2 \cdot \exp(\Gamma_2 \cdot t)$$

where  $A_{1,2}$  are amplitudes and  $\Gamma_{1,2} = -\tau_{1,2}^{-1}$ , where  $\tau$  is the lifetime. The fitting neglects the first part of the decay curve that appears due to instrument response, which is negligible compared to the reported lifetimes. Time-resolved fluorescence measurements were performed for all three PDI crystals (EP-PDI, PDI-Br<sub>2</sub>, and DMP-PDI) deposited on glass, on PVD films of CuPc, and decorated with CuPc crystalline leaflets. A biexponential fit to the lifetime curves yielded in two lifetimes, one short and one long. This can indicate that there are a few emitting populations; we neglected the longer lifetime components due to their small amplitudes and thus small contribution (at least one order of magnitude smaller than the amplitudes of the short lifetime components).

#### **Fabrication of ONCs films.**

ONCs of EP-PDI: A  $1 \times 10^{-3}$  M solution of EP-PDI in 7:3 (v/v) double-distilled water:tetrahydrofuran (DDW:THF) was prepared by dissolving EP-PDI in THF followed by dropwise addition of DDW (Barnstead NANO pure Diamond water system). This solution was sonicated for 10 minutes, and then 1 eq. of EP-PDI dissolved in 100  $\mu$ L of THF was injected rapidly, and aged in a sealed vial for several hours to give fibrous ONCs.

ONCs of PDI-Br<sub>2</sub>: A  $1 \times 10^{-4}$  M solution of PDI-Br<sub>2</sub> in 7:3 (v/v) DDW:THF was prepared by dissolving the solid compound in 200  $\mu$ L of THF and slowly injecting into DDW. This solution was sonicated for 10 minutes, added to a mixture of DDW and THF to give the final concentration, and aged in a sealed vial for several days to give fibrous ONCs.

ONCs of DMP-PDI: A  $1 \times 10^{-4}$  M solution of DMP-PDI in 6:4 (v/v) DDW:THF was prepared by dissolving DMP-PDI in THF, followed by rapid addition of DDW, and subsequent sonication for 10 minutes. Aging in sealed vials for several hours afforded platelet ONCs.

ONCs of CuPc: A  $1 \times 10^{-4}$  M solution of CuPc in 1:3:4 (v/v/v) DDW:acetone:TFA was by dissolving CuPc powder in 2 mL of TFA, followed by the slow additions of acetone and DDW. This solution was sonicated for 10 minutes and aged in a sealed vial for several days giving ONCs.

ONCs of CuPc-decorated PDIs: Starting with the solution of CuPc ONCs in DDW/acetone/TFA mixture, several rounds of solvent exchange replaced the solvent with *iso*-propanol. PDI ONCs were prepared as described above, then the extra solvent was removed to a minimal volume and then mixed with the *iso*-propanol solution of CuPc to give the desired 1:10 molar ratio of CuPc:PDI.

**Density Functional Theory (DFT) Calculation:** The coupling between two DMP-PDI molecules was considered using density functional theory and has been previously reported by us.<sup>S1</sup> From the crystal structures,  $\pi$ - $\pi$  stack dimers of EP-PDI and PDI-Br<sub>2</sub> were extracted and the locations of the hydrogen atoms were optimized at the DF-TPSS<sub>D3BJ</sub>/def2-SVP/W06 level of theory. It should be noted that the unit cell of PDI-Br<sub>2</sub> has two isomers with different Br substitutions (in roughly an 86:14 ratio) and only the major isomer was considered. Deng and Goddard derived a formula for the coupling matrix element  $V$  between two identical monomers,  $V = \frac{1}{2}(E_{HOMO} - E_{HOMO-1})$  where  $E$  is the energy of the HOMO or HOMO-1 molecular orbital of the dimer.<sup>S2</sup> The results are given in Table S4.

*Computational Methods:* The geometry of DMP-PDI was optimized using the Tao–Perdew–Staroverov–Scuseria (TPSS) exchange-correlation functional with an empirical dispersion correction added<sup>S3-6</sup>, specifically the third version of Grimme’s dispersion<sup>S3,7</sup> with Becke-Johnson dampening (D3BJ)<sup>S7-9</sup>; this combination is denoted as TPSSD3BJ. The use of a dispersion correction is essential to properly describe a system where the interactions between the two fragments are best described as “dispersion.”<sup>S10</sup> With this functional the second revision (def2) of Ahlrichs and coworkers’ basis sets<sup>S11-12</sup> (def2-SVP)<sup>S13-17</sup> was used. When using a GGA functional, a density fitting basis set, specifically Weigend-06 (W06) fitting set, was used to speed up the calculation. Only the hydrogen atoms were optimized. DFT calculations were run using GAUSSIAN16 REVISION B.01.<sup>S18</sup>

**Single Crystal Structure Analysis:** A PDI-Br<sub>2</sub> crystal was transferred to Paratone oil (Hampton Research), mounted on a MiTeGen loop, and flash frozen in liquid nitrogen. Crystal data for the PDI-Br<sub>2</sub>, measured at 100 K on a Rigaku XtaLabPro diffractometer equipped with [ $\lambda(\text{CuK}\alpha) = 0.154\ 184\ \text{\AA}$ ] radiation and a Dectris Pilatus S200 detector, was processed with CrysAlisPro programs (Rigaku). The structure was solved by direct methods with SHELXT-2016/4 and refined with full-matrix least squares

refinement based on F2 with SHELXL-2016/4. There are two independent molecules per asymmetric unit. The Br atoms on the molecules are discretely disordered. The occupancy of these Br atoms has been refined with 0.923/0.077 and 0.862/0.138 (for the two molecules respectively) with the vast majority of the molecules in having the Br atoms as shown in Figure 1a. The results are included in Table S5.

**Table S1.** Photovoltage ( $V_{PV}$ , V) measured by KPFM under laser and LED illumination for three configurations of PDI/CuPc interfaces. Standard deviation in brackets.

Materials	$V_{PV}$ (V)	NC/PVD	decorated	PVD/PVD
EP-PDI	Laser	0.45 (0.10)	0.28 (0.06)	0.28 (0.03)
	LED	0.08 (0.07)	0.066 (0.066)	0.17 (0.02)
PDI-Br <sub>2</sub>	Laser	0.65 (0.10)	0.35 (0.07)	0.53 (0.07)
	LED	0.39 (0.11)	0.11 (0.08)	0.13 (0.03)
DMP-PDI	Laser	0.53 (0.06)	— <sup>a</sup>	— <sup>a</sup>
	LED	0.58 (0.04)	— <sup>a</sup>	— <sup>a</sup>

<sup>a</sup> Not available; see text.

**Table S2.** The voltage loss ( $V_{loss}$ , V) in nanocrystal films calculated according to charge-transfer energy  $\Delta E_{DA}$  obtained from the PDI and CuPc frontier orbital energies.

Materials	$V_{loss}$ (V)	NC/PVD	decorated	PVD/PVD
EP-PDI	Laser	0.15	0.32	0.32
	LED	0.52	0.53	0.43
PDI-Br <sub>2</sub>	Laser	0.05	0.35	0.17
	LED	0.31	0.59	0.57
DMP-PDI	Laser	0.27	— <sup>a</sup>	— <sup>a</sup>
	LED	0.22	— <sup>a</sup>	— <sup>a</sup>

<sup>a</sup> Not available; see text.

**Table S3.** Photoluminescence exciton lifetime (ns) of PDIs from time-resolved fluorescence measurements. Standard deviation in brackets. Excitation wavelength is 470 nm.

Material	NC				NC/PVD				decorated			
	$\tau_1$ (ns)	A <sub>1</sub>	$\tau_2$ (ns)	A <sub>2</sub>	$\tau_1$ (ns)	A <sub>1</sub>	$\tau_2$ (ns)	A <sub>2</sub>	$\tau_1$ (ns)	A <sub>1</sub>	$\tau_2$ (ns)	A <sub>2</sub>
EP-PDI	<b>1.13</b>	1.14e7	3.32	2.44e4	— <sup>a</sup>				<b>1.12</b>	7.39e5	3.30	1.15e4
	(0.31)	(2.77e7)	(0.64)	(1.91e4)					(0.20)	(4.75e5)	(0.29)	(8.12e3)
PDI-Br <sub>2</sub>	<b>0.70</b>	2.38e8	1.73	2.91e5	— <sup>a</sup>				<b>0.66</b>	8.21e8	1.72	1.53e5
	(0.18)	(2.73e8)	(0.20)	(2.67e5)					(0.12)	(1.97e9)	(0.18)	(1.39e5)
DMP-PDI	<b>1.06</b>	2.19e7	3.65	4.62e4	<b>0.95</b>	3.59e6	3.38	5.74e3	<b>0.71</b>	3.88e7	2.29	2.13e4
	(0.19)	(3.18e7)	(0.54)	(3.90e4)	(0.13)	(2.42e6)	(0.34)	(1.81e3)	(0.10)	(5.79e7)	(0.24)	(6.47e3)

<sup>a</sup> Not available; see text.

**Table S4.** Calculated electronic coupling matrix elements (all values in units of eV).

	$E_{\text{HOMO}}$	$E_{\text{HOMO}-1}$	$V$
EP-PDI	-5.59	-5.74	0.07
PDI-Br <sub>2</sub>	-5.67	-5.83	0.08

**Table S5.** Detailed data of single crystal structure of PDI-Br<sub>2</sub>.

Complex	PDI-Br <sub>2</sub>
CCDC Deposition #	1895631
Formula	C <sub>34</sub> H <sub>28</sub> Br <sub>2</sub> N <sub>2</sub> O <sub>4</sub>
Crystal description	Orange needle
Crystal size [mm <sup>3</sup> ]	0.12 x 0.01 x 0.01
FW [g mol <sup>-1</sup> ]	688.40
Space group	<i>P2<sub>1</sub>c</i>
Crystal system	monoclinic
a [Å]	20.5304(13)
b [Å]	14.6380(9)
c [Å]	20.2108(17)
α [°]	90.0
β [°]	110.779(8)
γ [°]	90.0
Cell volume [Å <sup>3</sup> ]	5678.8(8)
Z	8
λ [Å]	1.54184
Temp [°]	100 K
ρ <sub>caclcd</sub> [g.cm <sup>-3</sup> ]	1.610
μ [mm <sup>-1</sup> ]	3.978
No. of reflections	12342
No. of unique reflections	5136
2Θ <sub>max</sub> [°]	95.84
R <sub>int</sub>	0.0671
No. of parameters (restraints)	775(11)
Final R <sub>1</sub> /wR <sub>2</sub> <sup>a</sup>	0.0690/ 0.1858
Final R <sub>1</sub> /wR <sub>2</sub> <sup>b</sup>	0.0933/ 0.1976
Goof	1.096

<sup>a</sup> for data with  $I > 2\sigma(I)$ . <sup>b</sup> for all data.

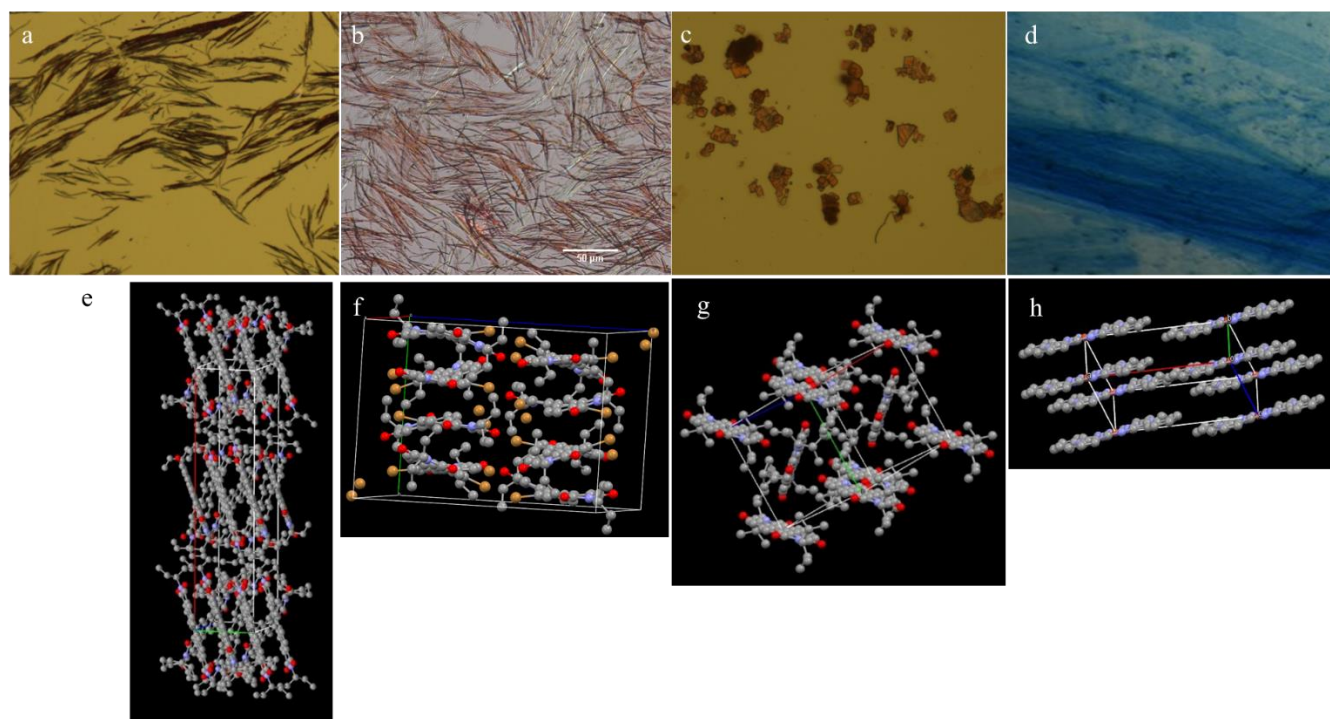


**Figure S1.** (a-d) Optical microscopic images of solution-processed Langmuir–Schaeffer films of ONCs and (e-h) single crystal structures of (a,e) EP-PDI, (b,f) PDI-Br<sub>2</sub>, (c,g) DMP-PDI and (d,h) CuPc.

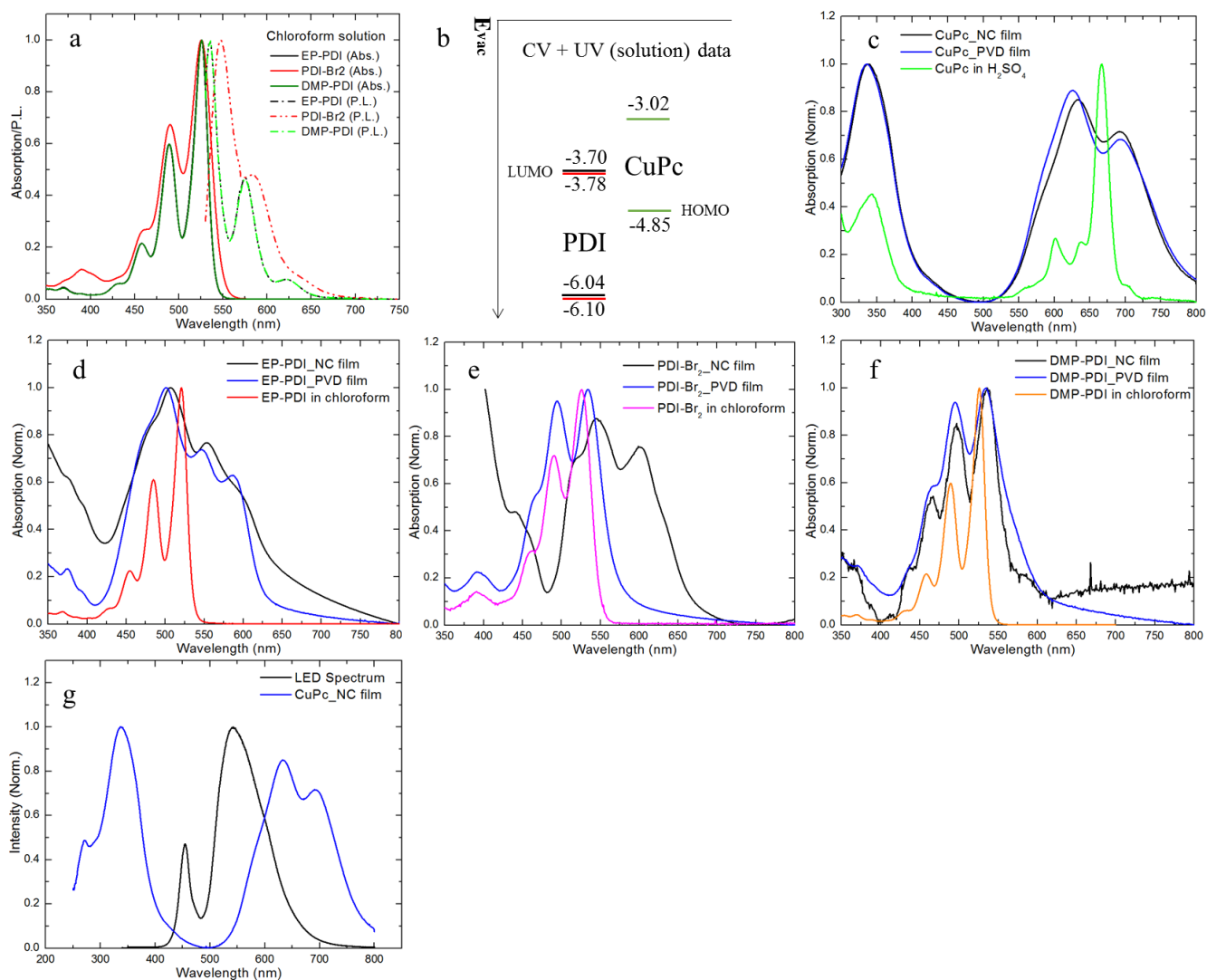


**Figure S2.** (a) UV-vis absorption and photoluminescence spectra of EP-DPI, PDI-Br<sub>2</sub> and DMP-DI in chloroform solution. (b) Frontier orbitals obtained by electrochemistry and optical bandgap of the molecules in solution, black for EP- and DMP-PDI (same orbital energies) and red for PDI-Br<sub>2</sub> respectively. (c-f) UV-vis absorption spectra of CuPc, EP-PDI, PDI-Br<sub>2</sub> and DMP-PDI, respectively, in solution and as films prepared by PVD or Langmuir-Schaefer films of nanocrystals (NC). (g) The spectrum of the LED used for illumination in this work, with the absorption spectrum of the CuPc film for comparison.

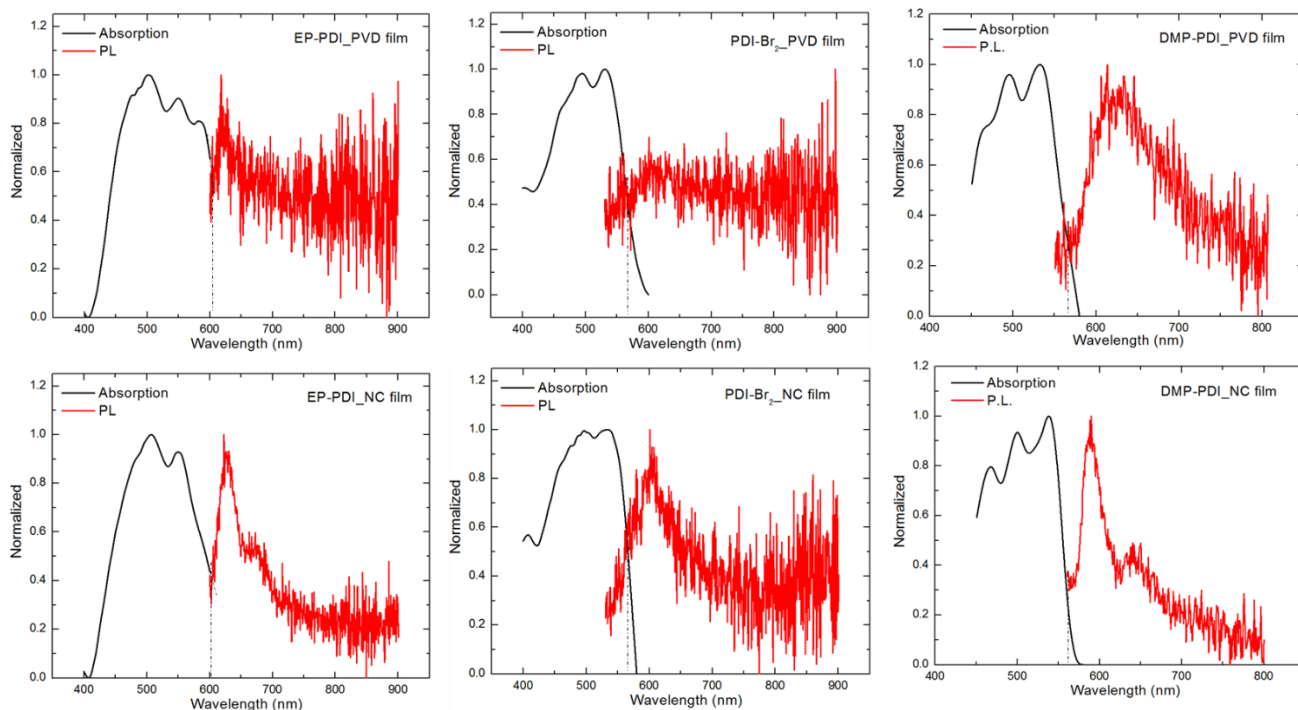


**Figure S3.** Absorption and photoluminescence of different PDI films (PVD: physical vapor deposition, NC: nanocrystal). The dashed line marks the crossing point of absorption and PL spectra.

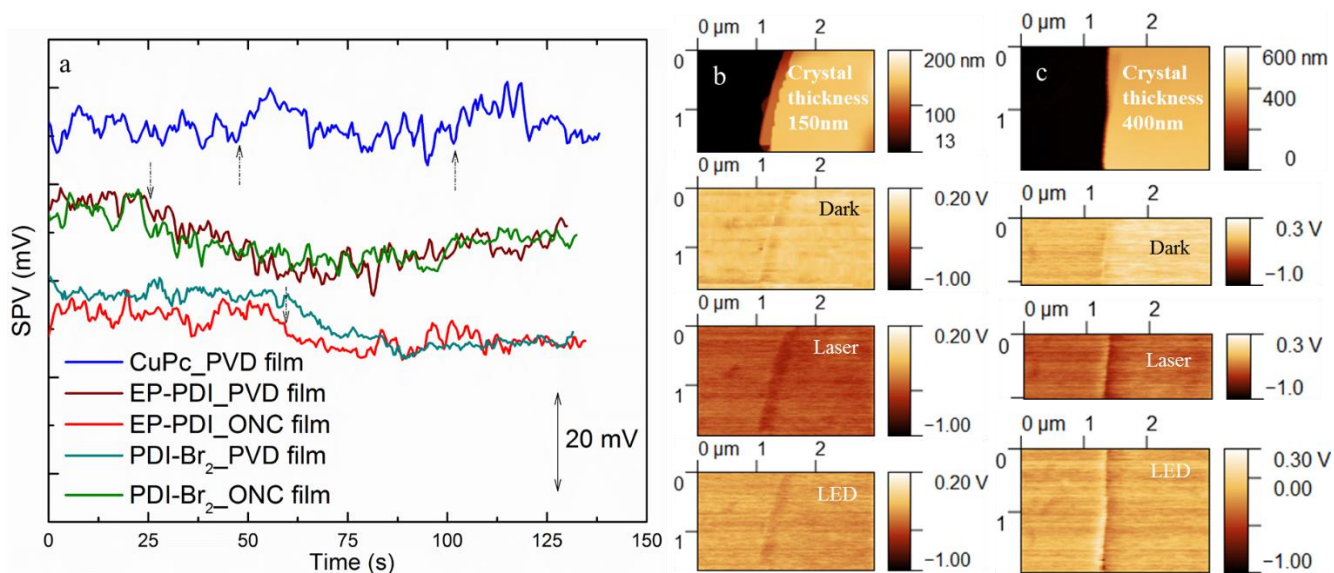


**Figure S4.** (a) Surface photovoltage (SPV) signals from macroscopic CPD measurements of PDIs and CuPc films on Au substrates. White light illumination (Xe lamp) is turned on at points indicated by the arrows, and the duration of illumination is about 20 seconds after the voltage stabilizes. (b) and (c) are KPFM measurements of DMP-PDI nanocrystals (150 and 400 nm thick, respectively) on bare gold substrates.

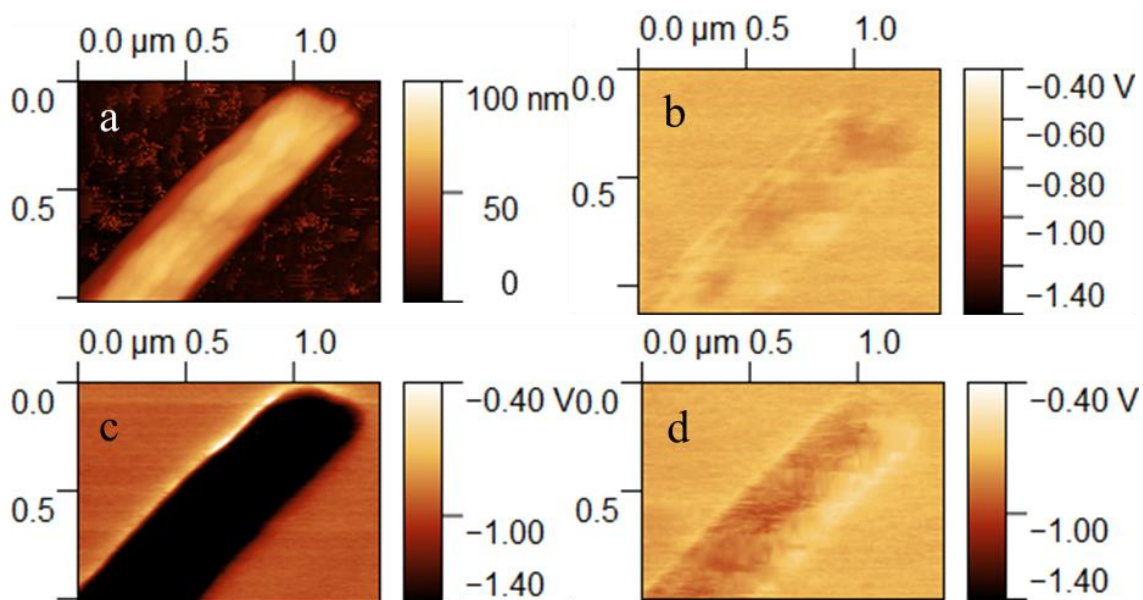


**Figure S5.** KPFM measurement of an EP-PDI nanocrystal on a CuPc PVD film (Configuration-I): (a) topography image (b-d) CPD signals in the dark, under laser illumination and under LED illumination, respectively. The crystal thickness is 80 nm.

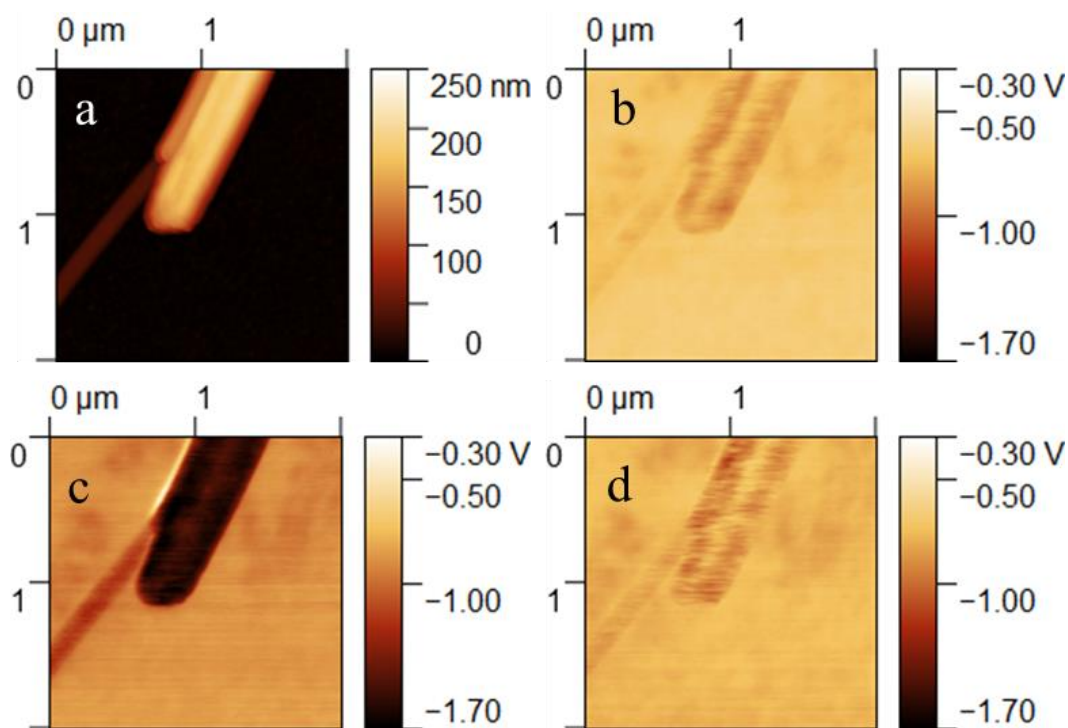


**Figure S6.** KPFM measurement of two EP-PDI nanocrystals on a CuPc PVD film (Configuration-I): (a) topography image (b-d) CPD signals in the dark, under laser illumination and under LED illumination, respectively. The crystal thicknesses are 70 nm (left) and 180 nm (right).

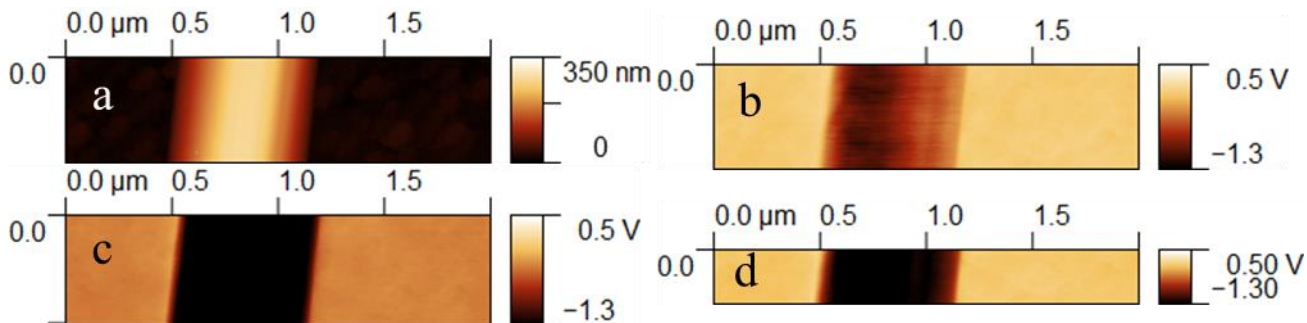


**Figure S7.** KPFM measurement of a PDI-Br<sub>2</sub> nanocrystal on a CuPc PVD film (Configuration-I): (a) topography image (b-d) CPD signals in the dark, under laser illumination and under LED illumination, respectively. The crystal thickness is 270 nm.

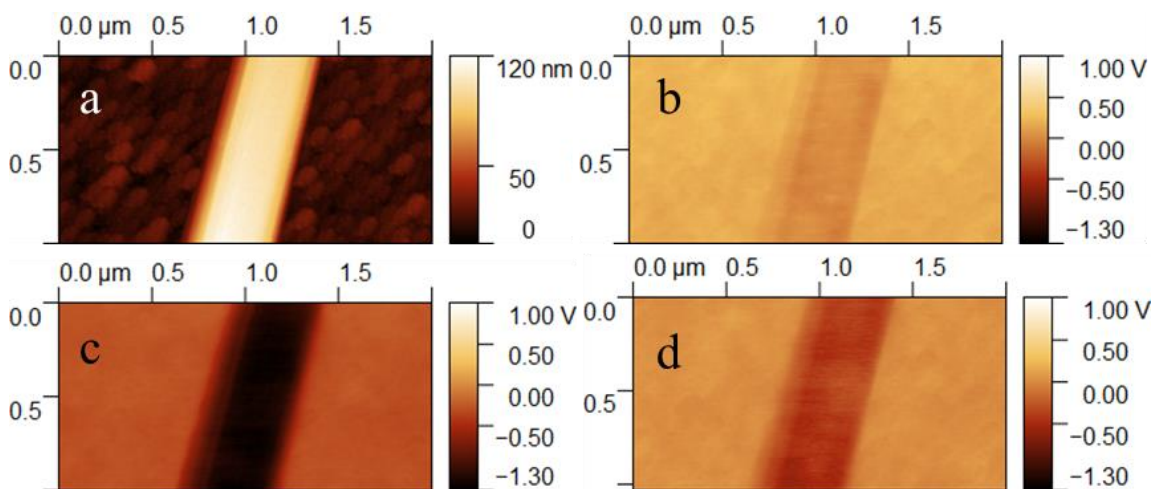


**Figure S8.** KPFM measurement of a PDI-Br<sub>2</sub> nanocrystal on a CuPc PVD film (Configuration-I): (a) topography image (b-d) CPD signals in the dark, under laser illumination and under LED illumination, respectively. The crystal thickness is 70 nm.

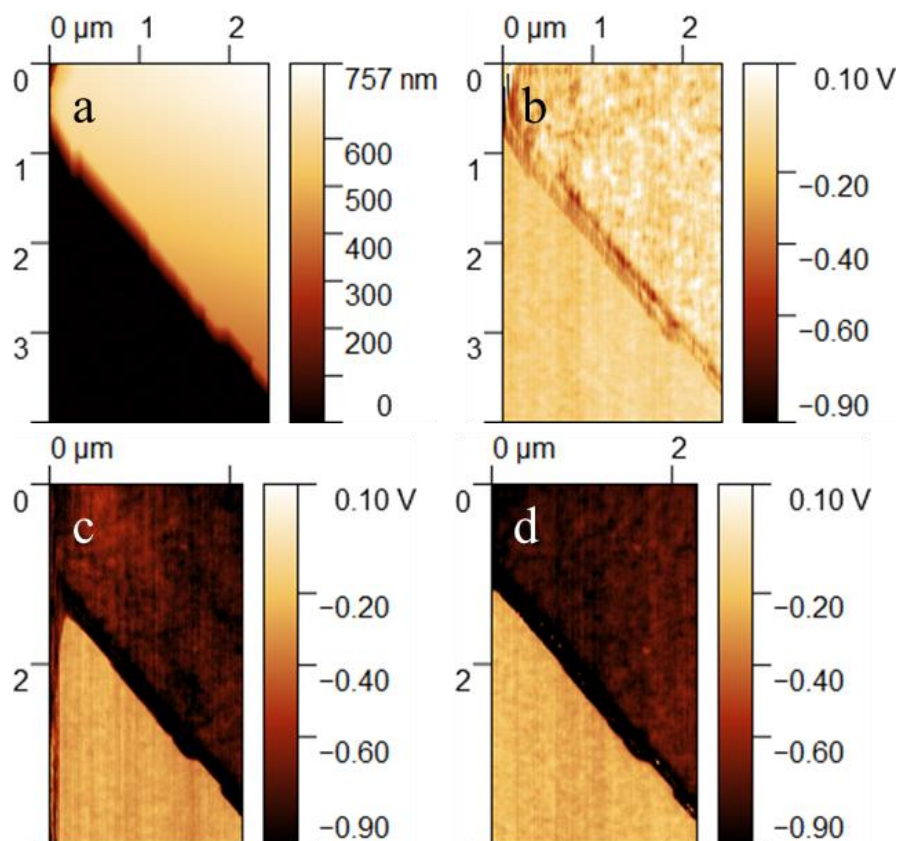


**Figure S9.** KPFM measurement of a DMP-PDI nanocrystal on a CuPc PVD film (Configuration-I): (a) topography image (b-d) CPD signals in the dark, under laser illumination and under LED illumination, respectively. The crystal thickness is 600 nm.

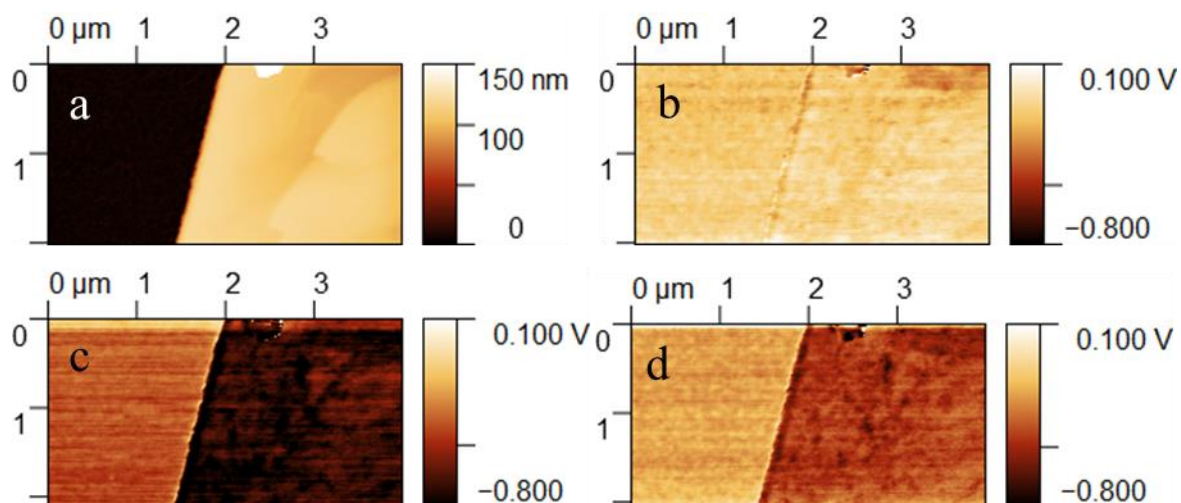


**Figure S10.** KPFM measurement of a DMP-PDI nanocrystal on a CuPc PVD film (Configuration-I): (a) topography image (b-d) CPD signals in the dark, under laser illumination and under LED illumination, respectively. The crystal thickness is 120 nm.

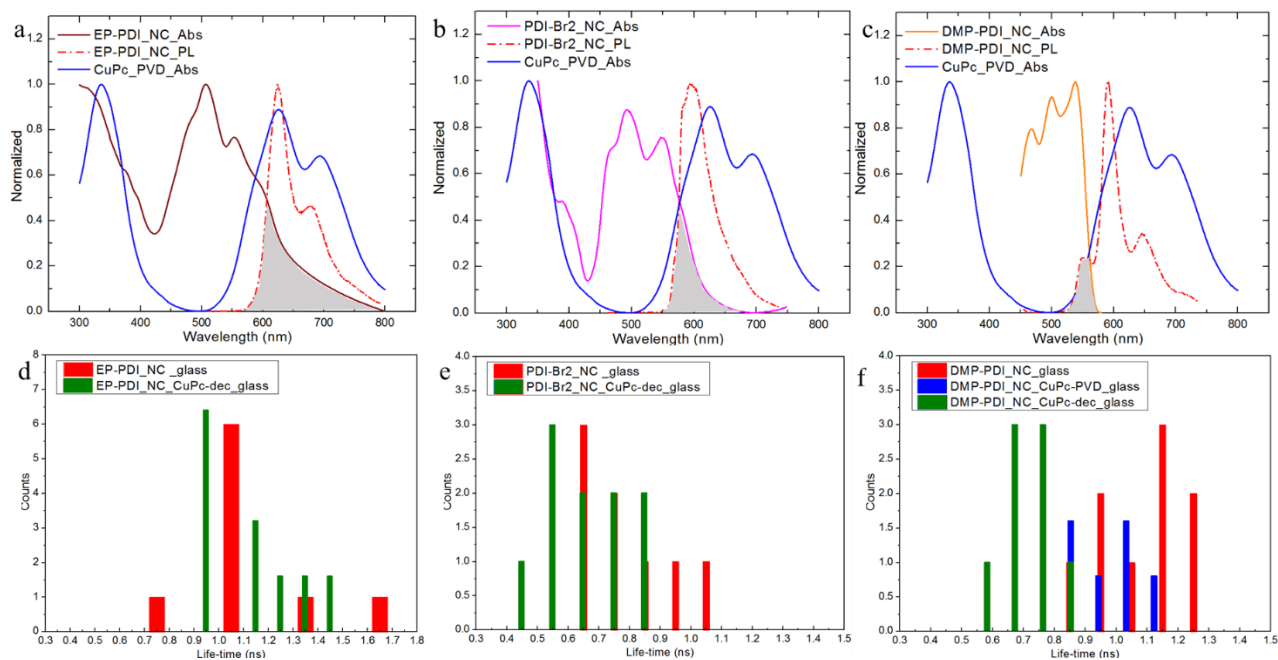


**Figure S11.** Photoabsorption (Abs.) and photoluminescence (PL) of (a) EP-PDI, (b) PDI-Br<sub>2</sub> and (c) DMP-PDI nanocrystals, as well as the absorption of CuPc PVD films. The gray area shows the self-absorption of PDI nanocrystals. (d-f) Histogram plots of PL life-time of (d) EP-PDI, (e) PDI-Br<sub>2</sub> and (f) DMP-PDI pristine nanocrystals and decorated with CuPc patches.

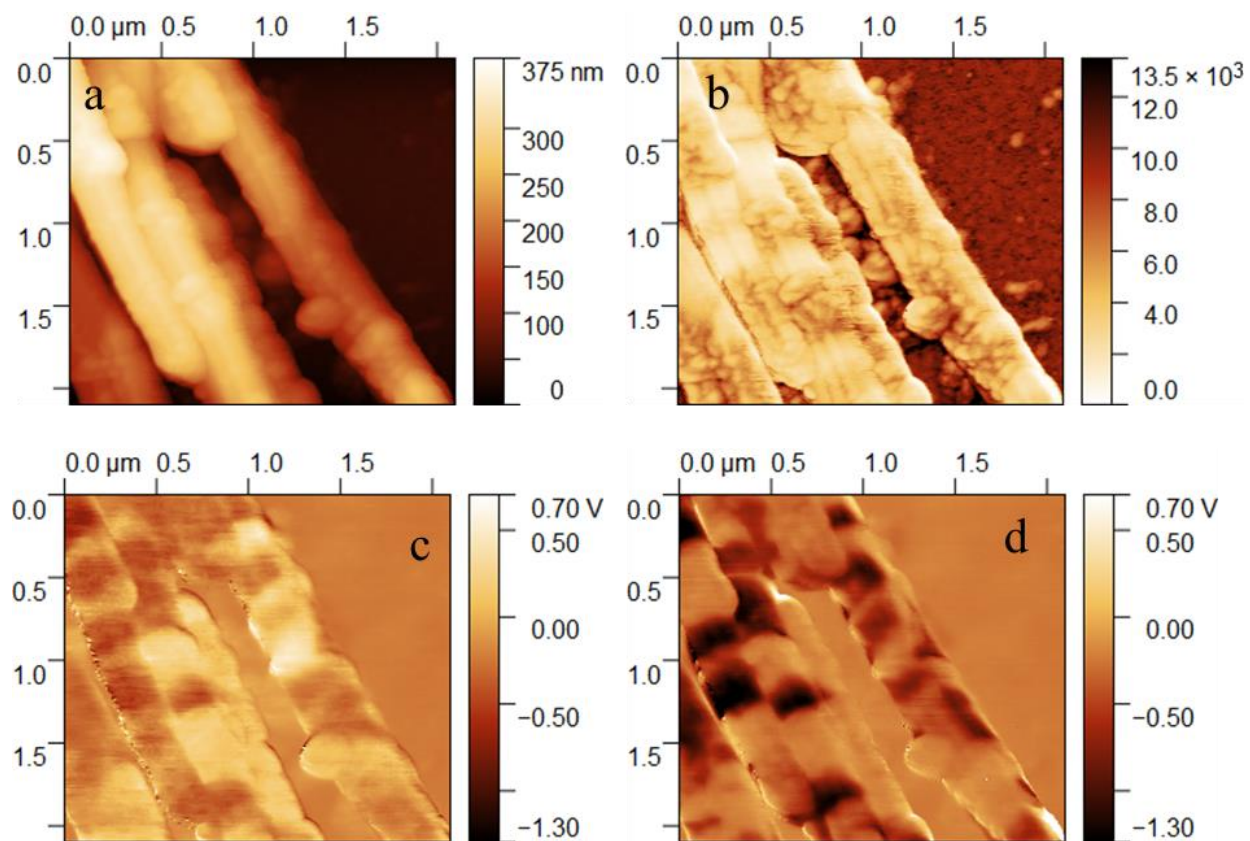


**Figure S12.** KPFM measurement of a PDI-Br<sub>2</sub> nanocrystal decorated with CuPc leaflets (Configuration-II): (a) topography image (b) the amplitude signal (y-axis in arbitrary units). (c) and (d) CPD signals in dark and under laser, respectively.

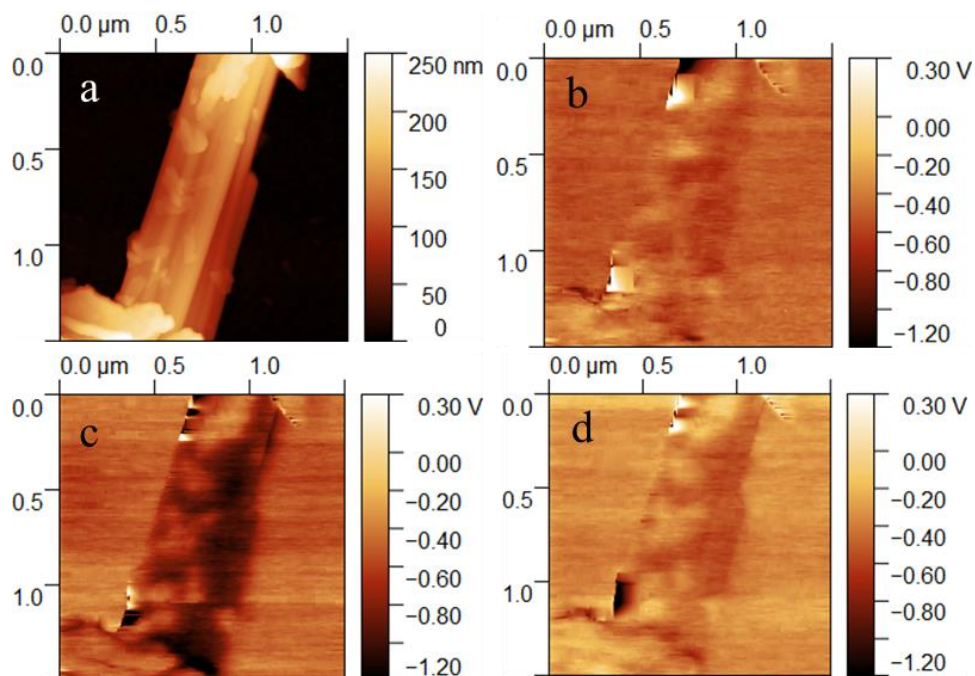


**Figure S13.** KPFM measurement of an EP-PDI nanocrystal decorated with CuPc leaflets (Configuration-II): (a) topography image, (b-d) CPD signals in the dark, under laser illumination and LED illumination, respectively. The thickness of the EP-PDI nanocrystal is about 100 nm.

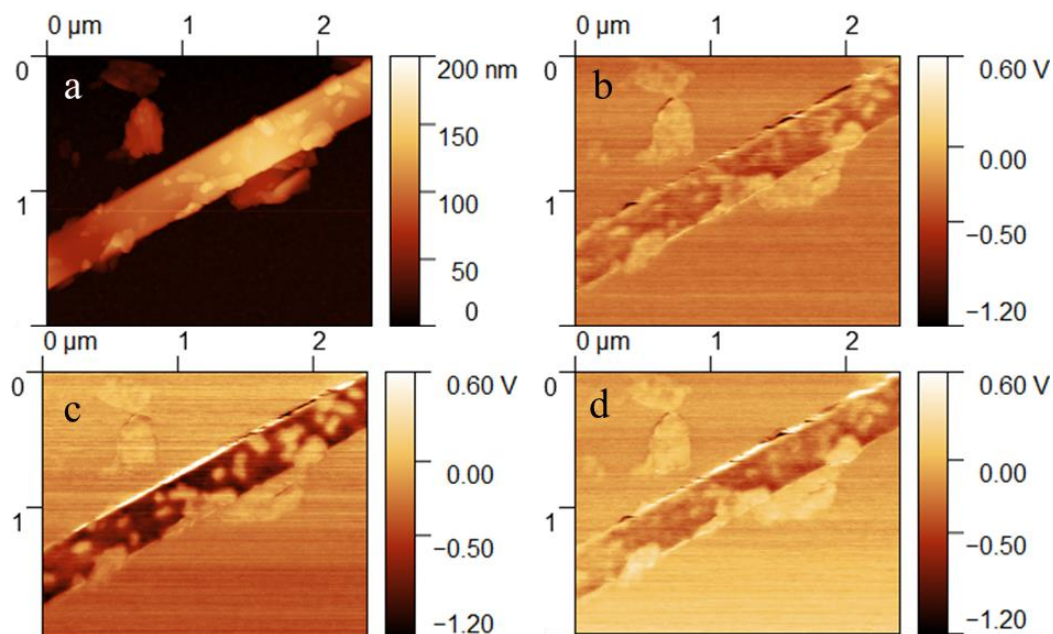


**Figure S14.** KPFM measurement of a PDI-Br<sub>2</sub> nanocrystal decorated with CuPc leaflets (Configuration-II): (a) topography image, (b-d) CPD signals in the dark, under laser illumination and LED illumination, respectively. The crystal thickness is about 60 nm.

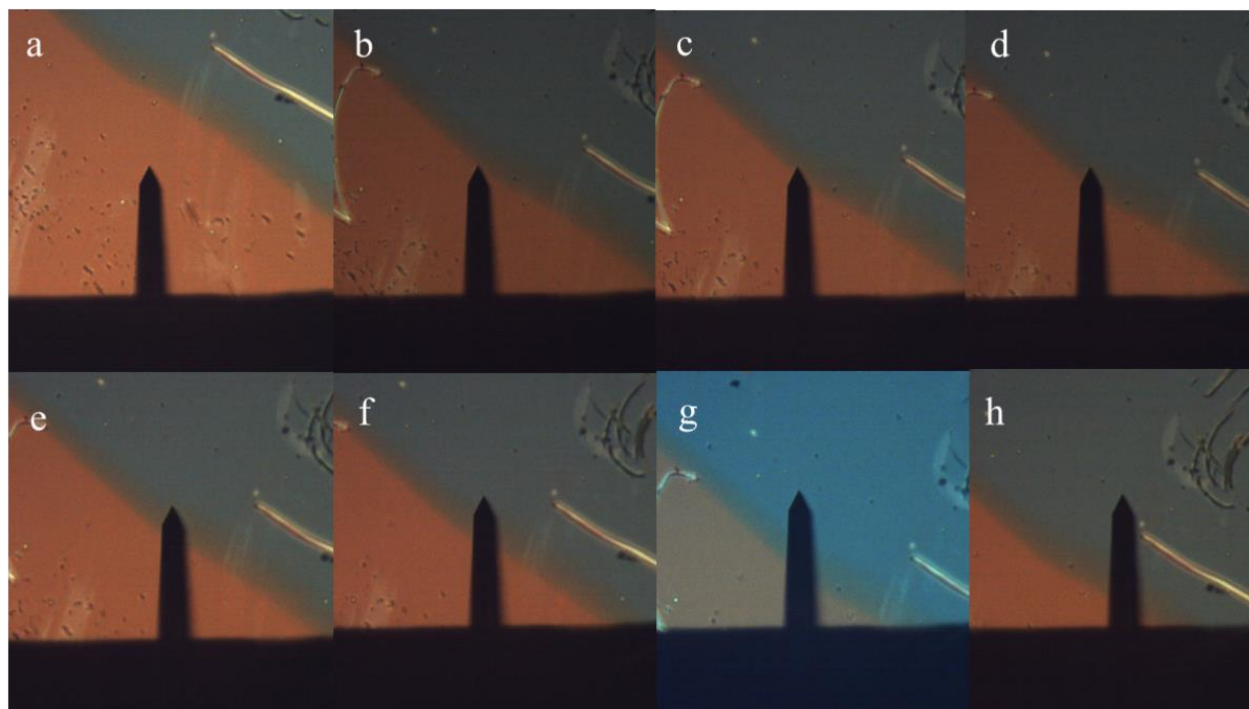


**Figure S15.** Optical microscopy images of the different positions during the KPFM measurements of an EP-PDI PVD layer overlaid by an offset CuPc PVD layer on a Au substrate (*i.e.*, Configuration-III).

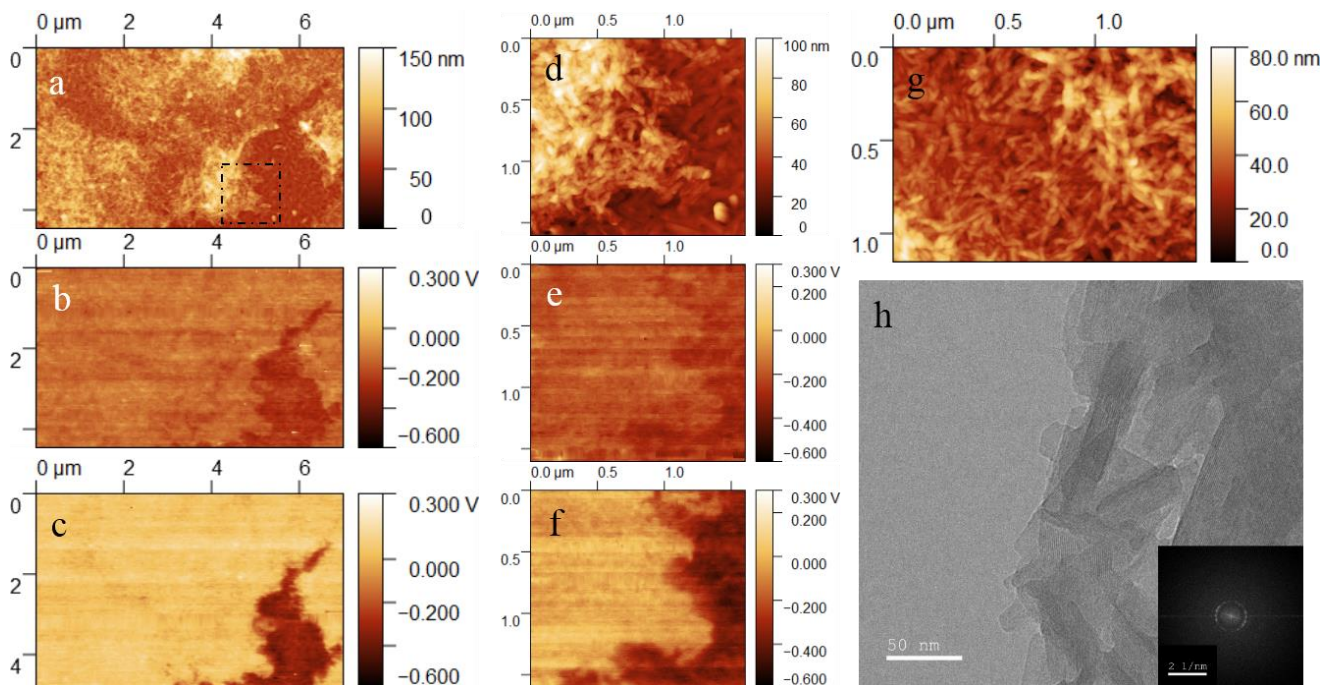


**Figure S16** Solution-processed CuPc crystalline patches deposited on an 80 nm thick EP-PDI PVD film on a gold substrate: (a) and (d) topography, (b) and (e) CPD signal in the dark, and (c) and (f) CPD signal under laser illumination; (d-f) are enlargements of the area indicated with dashed lines in (a). (g) and (h) are respectively the AFM and TEM images of the solution-processed CuPc nanocrystals. Inset in (h): Fast Fourier Transform (FFT, whole image). Observed spacing periodicities of the crystals are  $1.3 \pm 0.1$  nm.

As shown in Figure S16, the EP-PDI PVD layer has short-ribbon grains with lengths on the scale of 100 nm, in agreement with the XRD results (Figure 1j). The patches are composed of CuPc leaflets collected by the Langmuir–Schaeffer method. Films of the CuPc patches were of the  $\alpha$ -phase (Figures 1m and S2c) and showed the same WF and IP values as the PVD film (data not shown). According to eq. 2, the  $V_{PV}$  across the EP-PDI/CuPc interface (sharp interface, Figure S16d) equal to the difference in CPD contrast between the dark (Figure S16e) and laser (Figure S16f) scans was  $0.25 \pm 0.05$  V, comparable to the corresponding PVD bilayer results ( $0.28 \pm 0.03$  V, Table S1). TEM imaging (Figure S16h) shows that the solution-processed CuPc nanocrystals are in rectangular shape with the length along (010) axis and width along either (100) or (001) axis. These nanocrystals are assembled in the Langmuir–Schaeffer film with diverse orientations, as characterized by AFM (Figure S16g) and verified with powder XRD (Figure 1m).

## References

- S1. Bronshtein, I.; Iron, M. A.; Rybtchinski, B., Organic Phototransistors Based on Perylene Diimide Nanocrystals Lacking  $\pi$ - $\pi$  Interactions. *J. Mater. Chem. C* **2018**, *6*, 10597-10602.
- S2. Deng, W.-Q.; Goddard, W. A., III, Predictions of Hole Mobilities in Oligoacene Organic Semiconductors from Quantum Mechanical Calculations, *J. Phys. Chem. B* **2004**, *108*, 8614-8621.
- S3. Grimme, S.; Antony, J.; Ehrlich, S.; Kreig, H., A consistent and accurate ab initio parametrization of density functional dispersion correction (DFT-D) for the 94 elements H-Pu, *J. Chem. Phys.* **2010**, *132*, 154104.
- S4. Schwabe, T.; Grimme, S., Theoretical Thermodynamics for Large Molecules: Walking the Thin Line between Accuracy and Computational Cost, *Acc. Chem. Res.* **2008**, *41*, 569-579.
- S5. Schwabe, T.; Grimme, S., Double-hybrid density functionals with long-range dispersion corrections: higher accuracy and extended applicability, *Phys. Chem. Chem. Phys.* **2007**, *9*, 3397-3406.
- S6. Grimme, S., Semiempirical GGA-type density functional constructed with a long-range dispersion correction, *J. Comput. Chem.* **2006**, *27*, 1787-1799.
- S7. Grimme, S.; Ehrlich, S.; Goerigk, L., Effect of the damping function in dispersion corrected density functional theory, *J. Comput. Chem.* **2011**, *32*, 1456-1465.
- S8. Johnson, E. R.; Becke, A. D., A post-Hartree-Fock model of intermolecular interactions: Inclusion of higher-order corrections," *J. Chem. Phys.* **2006**, *124*, 174104.
- S9. Johnson, E. R.; Becke, A. D., A post-Hartree-Fock model of intermolecular interactions," *J. Chem. Phys.* **2005**, *123*, 024101.
- S10. Klimeš, J.; Michaelides, A., Perspective: Advances and challenges in treating van der Waals dispersion forces in density functional theory," *J. Chem. Phys.* **2012**, *137*, 120901.
- S11. Schäfer, A.; Horn, H.; Ahlrichs, R., Fully optimized contracted Gaussian basis sets for atoms Li to Kr, *J. Chem. Phys.* **1992**, *97*, 2571-2577.
- S12. Schäfer, A.; Huber, C.; Ahlrichs, R., Fully optimized contracted Gaussian basis sets of triple zeta valence quality for atoms Li to Kr, *J. Chem. Phys.* **1994**, *100*, 5829-5835.

- S13. Andrae, D.; Häußermann, U.; Dolg, M.; Stoll, H.; Preuß, H., Energy-adjusted ab initio pseudopotentials for the second and third row transition elements, *Theor. Chim. Acta* **1990**, *77*, 123-141.
- S14. Kaupp, M.; Schleyer, P. v. R.; Stoll, H.; Preuss, H., Pseudopotential approaches to Ca, Sr, and Ba hydrides. Why are some alkaline earth MX<sub>2</sub> compounds bent?, *J. Chem. Phys.* **1991**, *94*, 1360-1366.
- S15. Leininger, T.; Nicklass, A.; Küchle, W.; Stoll, H.; Dolg, M.; Bergner, A., The accuracy of the pseudopotential approximation: non-frozen-core effects for spectroscopic constants of alkali fluorides XF (X = K, Rb, Cs), *Chem. Phys. Lett.* **1996**, *255*, 274-280.
- S16. Metz, B.; Stoll, H.; Dolg, M., Small-core multiconfiguration-Dirac-Hartree-Fock-adjusted pseudopotentials for post-d main group elements: Application to PbH and PbO, *J. Chem. Phys.* **2000**, *113*, 2563-2569.
- S17. Weigend, F.; Ahlrichs, R., Balanced basis sets of split valence, triple zeta valence and quadruple zeta valence quality for H to Rn: Design and assessment of accuracy, *Phys. Chem. Chem. Phys.* **2005**, *7*, 3297-3305.
- S18. Gaussian 16, Revision B.01, M. J. Frisch, G. W. Trucks, H. B. Schlegel, G. E. Scuseria, M. A. Robb, J. R. Cheeseman, G. Scalmani, V. Barone, G. A. Petersson, H. Nakatsuji, X. Li, M. Caricato, A. V. Marenich, J. Bloino, B. G. Janesko, R. Gomperts, B. Mennucci, H. P. Hratchian, J. V. Ortiz, A. F. Izmaylov, J. L. Sonnenberg, D. Williams-Young, F. Ding, F. Lipparini, F. Egidi, J. Goings, B. Peng, A. Petrone, T. Henderson, D. Ranasinghe, V. G. Zakrzewski, J. Gao, N. Rega, G. Zheng, W. Liang, M. Hada, M. Ehara, K. Toyota, R. Fukuda, J. Hasegawa, M. Ishida, T. Nakajima, Y. Honda, O. Kitao, H. Nakai, T. Vreven, K. Throssell, J. A. Montgomery, Jr., J. E. Peralta, F. Ogliaro, M. J. Bearpark, J. J. Heyd, E. N. Brothers, K. N. Kudin, V. N. Staroverov, T. A. Keith, R. Kobayashi, J. Normand, K. Raghavachari, A. P. Rendell, J. C. Burant, S. S. Iyengar, J. Tomasi, M. Cossi, J. M. Millam, M. Klene, C. Adamo, R. Cammi, J. W. Ochterski, R. L. Martin, K. Morokuma, O. Farkas, J. B. Foresman, and D. J. Fox, Gaussian, Inc., Wallingford CT, 2016.